# Fluorescence Correlation Spectroscopy in Small Cytosolic Compartments Depends Critically on the Diffusion Model Used

Arne Gennerich and Detlev Schild
Physiologisches Institut, Universität Göttingen, D 37073 Göttingen, Germany

ABSTRACT Fluorescence correlation spectroscopy (FCS) is a powerful technique for measuring low concentrations of fluorescent molecules and their diffusion constants. In the standard case, fluorescence fluctuations are measured in an open detection volume defined by the confocal optics. However, if FCS measurements are carried out in cellular processes that confine the detection volume, the standard FCS model leads to erroneous results. In this paper, we derive a modified FCS model that takes into account the confinement of the detection volume. Using this model, we have carried out the first FCS measurements in dendrites of cultured neurons. We further derive, for the case of confined diffusion, the limits within which the standard two- and three-dimensional diffusion models give reliable results.

## INTRODUCTION

Fluorescence correlation spectroscopy (FCS) allows the measurement of nanomolar concentrations of fluorescent molecules and their diffusion constants (Widengren and Rigler, 1998). The method consists, first, of observing in a small illuminated sample volume fluorescence intensity fluctuations caused by concentration fluctuations and, second, of calculating the autocorrelation function (ACF) of the photodetector output. A theoretical model of the ACF is then fitted to the experimental ACF, yielding, as parameters, the average number $\langle N\rangle$ of molecules in the detection volume $V_d$ and the diffusion constant $D$. The model for free translational three-dimensional (3D) diffusion in the case of a 3D Gaussian approximation of the detectable emission intensity distribution (see Eq. 3) is given by (Aragón and Pecora, 1976; Rigler et al., 1993)

$$G(\tau) = \frac{1}{\langle N\rangle}\left(1 - \frac{I_B}{I_{tot}}\right)^2\left(1 + \frac{Te^{-\tau/\tau_T}}{1-T}\right) \times \frac{1}{1+\tau/\tau_{diff}}\cdot\frac{1}{\sqrt{1+\tau/S^2\tau_{diff}}}, \quad (1a)$$

where $T$ and $\tau_T$ account for the fractional part of molecules being in the triplet state and the triplet state decay time constant, respectively (Widengren et al., 1995); the factor $(1 - I_B/I_{tot})^2$ corrects for an uncorrelated background intensity $I_B$, with $I_{tot}$ being the total intensity including $I_B$ (Koppel, 1974); the steady state concentration of the fluorophore is $\langle C\rangle = \langle N\rangle/V_d$; the diffusion constant $D$ is related to the characteristic diffusion time constant $\tau_{diff}$ of the fluorescent molecules by $D = r_{xy}^2/4\tau_{diff}$; and $S$ equals the ratio $r_z/r_{xy}$ with $r_z$ and $r_{xy}$ being the distances in axial and lateral direction at which the intensity of the exciting laser beam is dropped by $1/e^2$, respectively.

In the case of $m$ noninteracting fluorescent species, the ACF consists of a weighted sum of individual ACFs as described by Eq. 1a

$$G(\tau) = \frac{1}{\langle N_{ges}\rangle}\left(1 - \frac{I_B}{I_{tot}}\right)^2\left(1 + \frac{Te^{-\tau/\tau_T}}{1-T}\right) \times \sum_{j=1}^{m}\frac{\Phi_j}{1+\tau/\tau_{diff_j}}\cdot\frac{1}{\sqrt{1+\tau/S^2\tau_{diff_j}}}. \quad (1b)$$

Here $\Phi_j$ is the fractional weighting factor for the $j$th species (Elson and Magde, 1974)

$$\Phi_j = \frac{Q_j^2 n_j}{(\sum_{j=1}^{m} Q_j n_j)^2}, \quad (1c)$$

where $Q_j$ is the quantum efficiency and $n_j = \langle N_j\rangle/\langle N_{ges}\rangle$ the relative molecular fraction.

In cases where the diffusion of one fluorescent species occurs in two dimensions, e.g., in the $x$–$y$ plane, Eq. 1a is simplified to a two-dimensional (2D) diffusion model,

$$G(\tau) = \frac{1}{\langle N\rangle}\left(1 - \frac{I_B}{I_{tot}}\right)^2\left(1 + \frac{Te^{-\tau/\tau_T}}{1-T}\right)\cdot\frac{1}{1+\tau/\tau_{diff}}. \quad (2a)$$

If the background intensity $I_B$ and triplet state population $T$ can be neglected, Eqs. 1a and 2a take on a simpler form,

$$G_{xyz}(\tau) := \frac{1}{\langle N\rangle}\cdot\frac{1}{1+\tau/\tau_{diff}}\cdot\frac{1}{\sqrt{1+\tau/S^2\tau_{diff}}}, \quad (1d)$$

and

$$G_{xy}(\tau) := \frac{1}{\langle N\rangle}\cdot\frac{1}{1+\tau/\tau_{diff}}. \quad (2b)$$

We set out to measure $\langle N\rangle$ and $D$ in cultured neurons of the olfactory bulb, in particular in small cytosolic compartments such as dendrites, to understand how the intracellular milieu affects the diffusion of fluorescent species in differ-

*Received for publication 17 April 2000 and in final form 26 June 2000.*
Address reprint requests to Detlev Schild, Universität Göttingen, Abt. Mol. Neurophysiologie, Humboldtallee 23, D-37073 Göttingen, Germany. Tel.: +49-551-39-5915; Fax: +49-551-39-8399; E-mail: dschild@gwdg.de.

0006-3495/00/12/3294/13 $2.00

ent parts of a cell. There are as yet few reports in which FCS has been applied to the intracellular environment (Berland et al., 1995; Politz et al., 1998; Brock et al., 1998; Schwille et al., 1999), none of them taking into account the specific geometry of the cellular compartments from which fluorescence was measured.

We here report that the models given by Eqs. 1 and 2 are generally not adequate to describe fluorescence correlation data taken in small cytosolic compartments. The reason is that the volume from which fluorescence is gathered is partly confined by the boundaries of the cell's plasma membrane rather than, as usually assumed, by the detection volume of the confocal optics. We have therefore developed a modified diffusion model that takes into account the extension of the cellular compartments from which fluorescence is gathered and, finally, confirm the validity of this model by applying it to small intracellular compartments of neurons of the olfactory bulb (OB) of *Xenopus laevis.*

## MATERIALS AND METHODS

### Cell culture

Cultured neurons of the OB of *Xenopus laevis* were prepared as described previously by Bischofberger and Schild (1995). Briefly, larvae of *X. laevis* (stage 48 to 54, Nieuwkoop and Faber, 1956) were anesthetized with Tricain (100 mg/l), and the olfactory bulbs were extirpated. The tissue was incubated at 22°C for 90 min in a dissociation solution containing EDTA (1 mM), papain (30 U/ml), and cysteine (1.5 mM). The resulting pieces were triturated with an Eppendorf pipette. The cells were plated onto dishes coated with poly-L-lysine (50 $\mu$g/ml) and laminin (20 $\mu$g/ml) in a drop of medium (50 $\mu$l) containing 70% L15, 10% horse serum, and 50 $\mu$g/ml gentamycin. After 20 h, 0.1 ml of growth medium, which contained 75% L15, 5% horse serum, and 50 $\mu$g/ml gentamycin, was added, allowing the cells to condition their own environment. Measurements were carried out within 2 weeks after plating.

The cultured cells were characterized with the use of antibodies against glial cells and GABAergic neurons. Mitral cells were identified by injection of fluorescent beads into the lateral olfactory tract and successive retrograde labeling (Bischofberger et al., 1995). The results were very similar to those reported for rat cultured OB cells (Trombley and Westbrook, 1990); mitral cells appeared as the largest neurons in the culture and were multipolar, whereas glutamic acid decarboxylase-positive cells were smaller and of ellipsoidal shape.

### Electrophysiology

To load the neurons with the fluorescent dye TMR-dextran (10 kDa, Sigma-Aldrich Chemie, Deisenhofen, Germany), the neurones were patch clamped in the whole cell configuration using borosilicate glass pipettes having pipette resistances of about 8 MΩ (the pipette solution contained the dye with a volume fraction of 1/100). Standard patch clamp equipment was used as described (Bischofberger and Schild, 1995). The composition of the bath solution was (in mM): NaCl 102, KCl 2, $MgCl_2$ 2, $CaCl_2$ 2, Glucose 20, HEPES 10, 240 mOsm, pH 7.8, while that of the pipette solution was NaCl 2, KCl 103, $MgCl_2$ 3, EGTA 1, HEPES 10, $K_2$-ATP 1, $Na_2$-GTP 0.01, 220 mOsm, pH 7.8.

### FCS set-up

The FCS set-up was similar to that described by Rigler et al. (1993), but differed in the following features: We used a HeNe cw-laser (2.2 mW) at 543.5 nm as excitation source (LK 54015, Laser Graphics, Dieburg, Germany). Tandem galvanometer mirrors (GD120DT, GSI Lumonics, Unterschleissheim, Germany) were used for *x–y*-positioning, and a piezo-driven objective holder (P-721.10, Physik Instrumente, Waldbronn, Germany) for *z*-positioning. The voltages to the *xy*-scanner and the *z*-piezo were controlled either by potentiometers or by a custom-made program written in C and running on a Siemens microcontroller (MCB-167, Keil Elektronik, Grasbrunn, Germany), to which a 12-bit dual-channel DAC (DAC 2813AP, Burr & Brown, Tucson, AZ) were latched. The back aperture of the objective used (C-Apochromat 40/1.2 W, Zeiss, Göttingen, Germany) was 9 mm. Because the laser beam diameter (double $1/e^2$ radius) at this aperture was 8.23 mm, the back aperture was not overilluminated. The detection pinhole had a diameter of 50 $\mu$m. The focal lengths of scanning and tube lens were such that the pinhole radius mapped into the object plane was about $r_{xy} = 0.24$ $\mu$m. The dark count rate of the avalanche

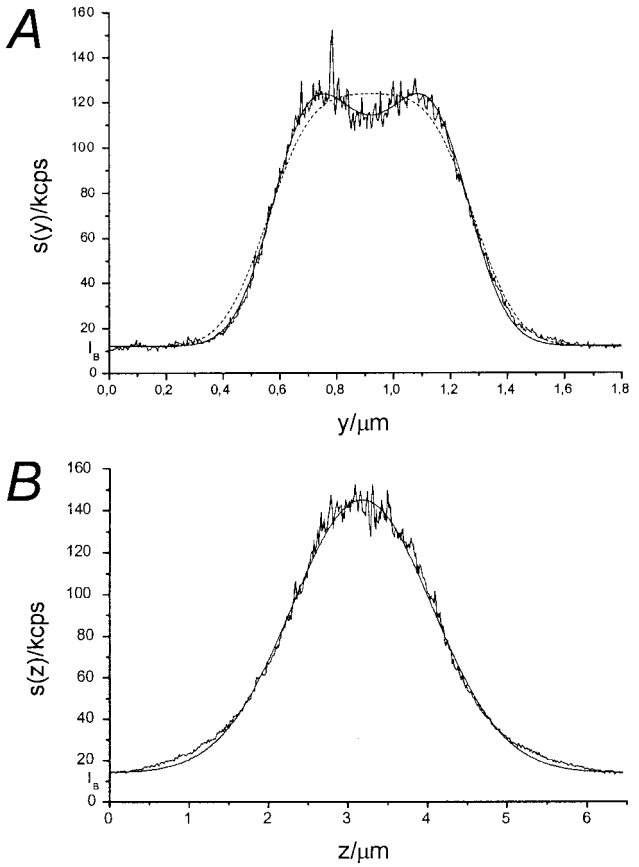


FIGURE 1 Line scanning profiles through two dendrites of a cultured neuron stained with the membrane dye di-8-ANNEPS. (*A*) *y*-scan (*noisy trace*); scan velocity of 32 nm/s. Fitting the rectangular profile (Eq. 9, *solid*) and the circular profile (Eq. 8, *dashed*) gave $d_y = 0.51$ $\mu$m, $d_z = 0.348$ $\mu$m, $\alpha_{rect.} = 47.52$ kcps, $d = 0.716$ $\mu$m, $\alpha_{circ.} = 60.5$ kcps, and $y_0 = 0.92$ $\mu$m, respectively. Fixed parameters: $r_{xy} = 0.25$ $\mu$m, $r_z = 1.73$ $\mu$m, and $I_B = 12$ kcps. (*B*) *z*-scan (*noisy trace*); scan velocity: 107.5 nm/s. Fitting the rectangular profile (Eq. 11, *solid*) gave $d_y = 0.424$ $\mu$m, $d_z = 0.553$ $\mu$m, $\alpha_{rect.} = 52.23$ kcps, and $z_0 = 3.18$ $\mu$m. Fixed parameters: $r_{xy} = 0.24$ $\mu$m, $r_z = 1.7$ $\mu$m, and $I_B = 14$ kcps. The tails of the data are not perfectly fitted by Eq. 11 due to the assumption that the detectable emission intensity distribution $I_E(\vec{r})$ (Eq. 3) has a 3D Gaussian shape, while the data still reflect the axial Lorezian shape of the exciting volume.

photodiode used (SPCM-AQ-141, EG&G, Optoelectronics, Dumberry, Canada) was 100 $s^{-1}$, its photon detection efficiency was 70–80%. Back-reflection ($\lambda_{exc}$ = 543.5 nm) was blocked by an interference filter (HQ 582/50, OD6, AF Analysetechnik, Pfrondorf, Germany) put in front of the photodiode. The output pulses of the photon-counting module were fed to a correlator board (ALV-5000/E, ALV, Langen, Germany).

The Gaussian laser beam profile and the pinhole used determined the detectable emission intensity distribution $I_E(\vec{r})$ (Rigler et al., 1993)

$$I_E(\vec{r}) = gQI_0 \exp\left(-2\frac{x^2+y^2}{r_{xy}^2}\right)\exp\left(-2\frac{z^2}{r_z^2}\right). \quad (3)$$

$g$ accounts for the overall optical losses of the emission pathway including the efficiency of the photoavalanchediode, and $Q$ is the quantum efficiency of the fluorescent dye. $I_0$ is the maximum laser intensity in the focus. This profile corresponds to the apparent closed detection volume $V_d$,

$$V_d = \pi^{3/2} r_{xy}^2 r_z, \quad (4)$$

from which fluorescence is gathered. The beam waist radius $r_{xy}$ and the structure factor $S$ was determined by measuring the translational 3D diffusion of TMR in water, assuming a diffusion constant of $D = 2.8 \times 10^{-6}$ $cm^2/s$ (Rigler et al., 1993).

## Size of dendrites

In this context, there are two reasons why it is important to measure the size of dendritic compartments. First, the concentration of fluorescent molecules can be calculated from the average particle number $\langle N\rangle$ in the sample volume only if the sample volume is known. In dendrites, the volume in which diffusion takes place is partly given by the plasma membrane boundaries, which therefore need to be estimated. The second reason is that the dendritic diameters in the diffusion model we develop herein result as fit parameters from the FCS analysis. An independent measurement of the dendritic size can confirm the diameters resulting from the diffusion model.

We used two ways of determining the dendritic size. The first way consists in staining the plasma membrane. After an FCS measurement, the cultured neurons were incubated for ~3 min in 20 $\mu$M di-8-ANNEPS (Molecular Probes, Leiden, the Netherlands) dissolved in the bath solution. After rinsing the bath, we scanned along a line orthogonal to the dendrite. An example of the resulting intensity profile is shown in Fig. 1 *A*. The dendritic diameters follow from the convolution analysis of the profile. A line-scanning profile is the convolution product of the excitation volume, approximately given by Eq. 3, and a boundary function $\xi(x, y, z)$ which is zero everywhere except at the plasma membrane. Because of the high membrane dye concentration, the cytosolic fluorescence contribution of the FCS measurement was neglected. Interestingly, fitting the scanned profile (Fig. 1 *A*) can provide information about the dendritic cross section. We first assumed a circular boundary function in the $y$–$z$-plane orthogonal to the dendrite,

$$\xi_{circ.}(y,z) = \int_{y_0-d/2}^{y_0+d/2} dy''\delta(y''-y)\left[\delta\left(z-\sqrt{\frac{d^2}{4}-(y''-y_0)^2}\right) + \delta\left(z+\sqrt{\frac{d^2}{4}-(y''-y_0)^2}\right)\right], \quad (5)$$

and, second, a rectangular function

$$\xi_{rect.}(y,z) = \int_{y_0-d_y/2}^{y_0+d_y/2} dy''\delta(y''-y)\left[\delta\left(z-\frac{d_z}{2}\right)+\delta\left(z+\frac{d_z}{2}\right)\right] + \int_{-d_z/2}^{d_z/2} dz''\delta(z''-z)\left[\delta\left(y-y_0+\frac{d_y}{2}\right) + \delta\left(y-y_0-\frac{d_y}{2}\right)\right], \quad (6)$$

with $y = y_0$ and $z = 0$ being the center of the dendritic cross section. The circular cross section is defined by the diameter $d$, whereas the rectangular cross section is defined by the width $d_y$ and the height $d_z$. Generally, $d$, $d_y$, and $d_z$ are slowly varying parameters along the dentrite.

The convolution of Eqs. 5 or 6 with the excitation volume (Eq. 3) gives the theoretical $y$-line scanning profile,

$$s(y) = \langle C_S\rangle \int_{-\infty}^{+\infty} dx' \int_{-\infty}^{+\infty} dy' \int_{-\infty}^{+\infty} dz' \xi(x', y', z') \cdot I_E(x', y-y', z'), \quad (7)$$

with $\langle C_S\rangle$ being the average number of dye molecules per surface element.

For a circular cross section, we have

$$s_{circ.}(y) = \alpha\cdot(1-S^{-2})^{-1/2} \times \exp\left\{-2\left[\frac{d^2/4-y_0^2}{r_z^2}+\frac{y^2}{r_{xy}^2}-\frac{(yS^2-y_0)^2}{r_z^2(S^2-1)}\right]\right\} \times \left\{\operatorname{erf}\left[\frac{\sqrt{2(S^2-1)}}{r_z}\left(y_0+\frac{d}{2}-\frac{yS^2-y_0}{S^2-1}\right)\right] - \operatorname{erf}\left[\frac{\sqrt{2(S^2-1)}}{r_z}\left(y_0-\frac{d}{2}-\frac{yS^2-y_0}{S^2-1}\right)\right]\right\}, \quad (8)$$

whereas, for a rectangular cross section, we obtain

$$s_{rect.}(y) = \alpha\cdot\left[\exp\left(-\frac{d_z^2}{2r_z^2}\right)\left\{\operatorname{erf}\left(\sqrt{2}\frac{y-y_0+d_y/2}{r_{xy}}\right) - \operatorname{erf}\left(\sqrt{2}\frac{y-y_0-d_y/2}{r_{xy}}\right)\right\} + S\cdot\operatorname{erf}\left(\frac{d_z}{\sqrt{2}r_z}\right)\right] \times \left\{\exp\left(-2\frac{(y-y_0+d_y/2)^2}{r_{xy}^2}\right) + \exp\left(-2\frac{(y-y_0-d_y/2)^2}{r_{xy}^2}\right)\right\}\Bigg], \quad (9)$$

where

$$\alpha = gQI_0\langle C_S\rangle\frac{\pi}{2}r_{xy}^2, \quad S = \frac{r_z}{r_{xy}}. \quad (10)$$

Fitting either function (Eqs. 8 and 9) to the data shown in Fig. 1 *A* revealed that the experimental profile is best described by rectangular

boundaries (the Gaussian error deviations of the theoretical curve from the experimental values were $\chi^2_{\text{circ.}} = 29.95$ and $\chi^2_{\text{rect.}} = 11.57$, respectively). This is presumably due to the typical shape of cultured cells, which is often rectangular at their bases due to the cell's adhesion to the Petri dish.

Similarly, the dendritic boundaries can be measured by scanning parallel to the optical axis using a calibrated piezo objective drive. Fig. 1 *B* shows a *z*-scan through a dendrite, centered at $y = 0$ and $z = z_0$, along with the theoretical profile for the rectangular approximation,

$$s_{\text{rect.}}(z) = \alpha \cdot \left[ S \cdot \exp\left( -\frac{d_y^2}{2r_{xy}^2} \right) \left\{ \text{erf}\left( \sqrt{2}\,\frac{z - z_0 + d_z/2}{r_z} \right) - \text{erf}\left( \sqrt{2}\,\frac{z - z_0 - d_z/2}{r_z} \right) \right\} + \text{erf}\left( \frac{d_y}{\sqrt{2} r_{xy}} \right) \times \left\{ \exp\left( -2\,\frac{(z - z_0 + d_z/2)^2}{r_z^2} \right) + \exp\left( -2\,\frac{(z - z_0 - d_z/2)^2}{r_z^2} \right) \right\} \right]. \quad (11)$$

The second way of determining the dendritic size consists in measuring a line scan orthogonal to a dendrite that is homogeneously filled with a hydrophilic dye. This method is useful if the emission intensity is sufficiently high to give smooth functions and if several cells are to be used in the same culture dish. Assuming a concentration $\langle C \rangle$ and a rectangular cross section,

$$\xi_{\text{rect.}}(y, z) = [\varepsilon(y - y_0 + d_y/2) - \varepsilon(y - y_0 - d_y/2)] \times [\varepsilon(z + d_z/2) - \varepsilon(z - d_z/2)], \quad (12)$$

with

$$\varepsilon(y - y_0) = \begin{cases} 1 & \text{for} \quad y \geq y_0 \\ 0 & \text{otherwise,} \end{cases} \quad (13)$$

the line-scanning profile in the image plane is

$$s'_{\text{rect.}}(y) = \beta \cdot \left[ \text{erf}\left( \sqrt{2}\,\frac{y - y_0 + d_y/2}{r_{xy}} \right) - \text{erf}\left( \sqrt{2}\,\frac{y - y_0 - d_y/2}{r_{xy}} \right) \right] \quad (14)$$

with

$$\beta = gQI_0\langle C \rangle r_{xy}^2 r_z \frac{\pi^{3/2}}{2^{5/2}} \text{erf}\left( \frac{d_z}{\sqrt{2} r_z} \right), \quad (15)$$

while line scanning along the optical axis is

$$s'_{\text{rect.}}(z) = \gamma \cdot \left[ \text{erf}\left( \sqrt{2}\,\frac{z - z_0 + d_z/2}{r_z} \right) - \text{erf}\left( \sqrt{2}\,\frac{z - z_0 - d_z/2}{r_z} \right) \right], \quad (16)$$

with

$$\gamma = gQI_0\langle C \rangle r_{xy}^2 r_z \frac{\pi^{3/2}}{2^{5/2}} \text{erf}\left( \frac{d_y}{\sqrt{2} r_{xy}} \right). \quad (17)$$

## RESULTS

### Standard model

The fluctuation $\delta C(\vec{r}, t)$ of the local concentration $C(\vec{r}, t)$ at a point $\vec{r}$ and time $t$ occurs around the steady state concentration $\langle C \rangle$,

$$\delta C(\vec{r}, t) = C(\vec{r}, t) - \langle C \rangle. \quad (18)$$

The correlation of the concentration fluctuation $\delta C(\vec{r}, t)$ at $\vec{r}$ and $t$ with the concentration fluctuation $\delta C(\vec{r}', t + \tau)$ at $\vec{r}'$ and a later time $t + \tau$ is given by

$$\phi(\vec{r}, \vec{r}', t, \tau) = \langle \delta C(\vec{r}, t) \delta C(\vec{r}', t + \tau) \rangle, \quad (19)$$

or, assuming stationarity (Papoulis, 1991),

$$\phi(\vec{r}, \vec{r}', \tau) = \langle \delta C(\vec{r}, 0) \delta C(\vec{r}', \tau) \rangle. \quad (20)$$

$\phi$ can be expressed in terms of the probability density for a single molecule that started a random walk at time $\tau = 0$ at the point $\vec{r}$ to be at $\vec{r}'$ at time $\tau$,

$$\phi(\vec{r}, \vec{r}', \tau) = \langle C \rangle p(\vec{r}, \vec{r}', \tau), \quad (21)$$

with

$$p(\vec{r}, \vec{r}', \tau) = (4\pi D\tau)^{-3/2} \exp\left( -\frac{(\vec{r} - \vec{r}')^2}{4D\tau} \right). \quad (22)$$

The normalized 3D correlation function (Eq. 1) can be calculated from Eqs. 3, 21, and 22 (Aragón and Pecora, 1976). Note that the 3D autocorrelation function (Eq. 1d)

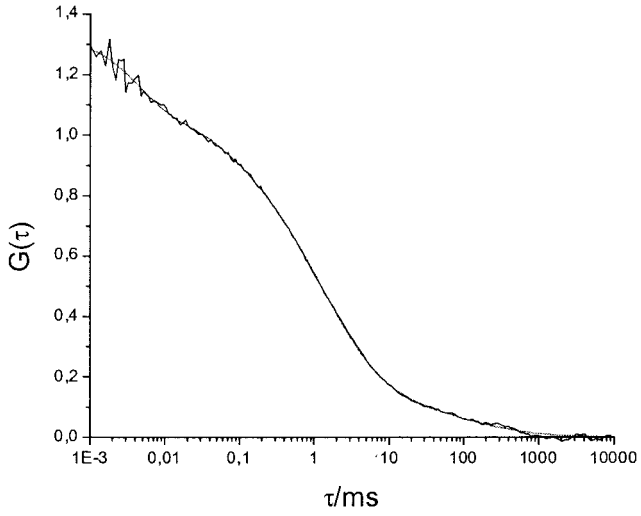


FIGURE 2 Autocorrelation curve calculated from fluorescence fluctuations of 10 kDa TMR-dextran emitted from a dentrite of a cultured neuron of the OB. The ACF was measured over 60 s after diffusion had reached a steady state. The dye concentration in the pipette was 20 nM and the maximum laser intensity in the focus was $I_0 = 3.14$ kW/cm$^2$. Fitting the standard multicomponent ACF model (Eq. 1b) gave $\langle N \rangle = 0.933$, $T = 0.192$, $\tau_T = 4.37$ $\mu$s, and the parameters given in the text. Fixed parameter: $S = 7$.

can be written as the reciprocal particle number times the product of three functions $g_i(\tau)$,

$$G_{xyz}(\tau) = \frac{1}{\langle N\rangle}\cdot\frac{1}{\sqrt{1+4D\tau/r_{xy}^2}}\cdot\frac{1}{\sqrt{1+4D\tau/r_{xy}^2}}\cdot\frac{1}{\sqrt{1+4D\tau/r_z^2}}$$
$$= \frac{1}{\langle N\rangle}\cdot g_x(\tau)\cdot g_y(\tau)\cdot g_z(\tau). \quad (23)$$

## Failure of the standard model

Figure 2 shows an autocorrelation function calculated from the fluorescence fluctuations of TMR-dextran (10 kDa) emitted from a dendrite of a cultured neuron of the OB. The dendrite's diameter was slightly smaller than 1 $\mu$m. Attempts to fit this autocorrelation function with the model given by Eq. 1a failed to converge. The fluorescence fluctuations of a fluorophore when injected into a cell can have more than one kinetic constant (Brock et al., 1998). Therefore we tried to fit the experimental autocorrelation function to the multi-component model (Eq. 1b). The simplest model describing the data (Fig. 2) was a three-component model. The first component contributed 25% with a time constant of $\tau_{diff_1} = 93.5$ $\mu$s, the second 68% with $\tau_{diff_2} = 1.51$ ms, and the third 7% with $\tau_{diff_3} = 154$ ms. The problem with this fit is that the characteristic time constant $\tau_{diff_1}$ is much smaller than the time constant of TMR-dextran (10 kDa) in water (about 0.16 ms for our FCS set-up). $\tau_{diff_1}$ is also much smaller than the measured characteristic diffusion times of the autofluorescent components (own data). Hence, the fit shown in Fig. 2, though numerically correct, lacks physical plausibility.

The reason for this obvious discrepancy lies in the morphology of the cell from which the fluorescence was recorded. Fig. 3 shows a laser scanning micrograph of a typical neuron of the OB. In the derivation of the standard FCS models (Eqs. 1 and 2), it is assumed that the volume within which diffusion occurs is much larger than the confocal detection volume from which fluorescence is recorded. In our system, the detection volume $V_d$ has $1/e^2$ radii of about $r_{xy} = 0.24$ $\mu$m and $r_z = 1.7$ $\mu$m, respectively. Obviously, the size of a dendrite can be of the same order or smaller. Therefore, the models given by Eq. 1 and 2 do not adequately describe data taken in small cytosolic compartments.

In the following, we develop a modified FCS model that takes boundaries such as the plasma membrane into account. We first consider the case where diffusion is confined in the axial direction of the detection volume and then extend the results to the case where diffusion is also confined in one lateral direction.

## Model of diffusion limited by boundaries in axial direction

We consider boundary planes at $z = 0$ and $z = d_z$ perpendicular to the optical axis such that diffusion is confined between these boundaries. For a 2D Gaussian intensity profile, this case has been treated in detail by Elson and Magde (1974). In the case of a 3D Gaussian intensity distribution (Eq. 3) the detectable diffusion takes place in a barrel-like volume (Fig. 4) rather than in an ellipsoid-like volume. As the diffusive flux vanishes at the boundaries, they expanded the concentration fluctuation $\delta C(\vec{r}, t)$ in a Fourier cosine series along the $z$-axis. After a number of algebraic steps and Fourier transforms, they showed that (Elson and Magde, 1974)

$$\phi(\vec{r}, \vec{r}', \tau) = \langle C\rangle p_{xy} p_{z^*}, \quad (24)$$

where

$$p_{xy}(x, x', y, y', \tau)$$
$$= (4\pi D\tau)^{-1}\exp(-[(x-x')^2 + (y-y')^2]/4D\tau) \quad (25)$$

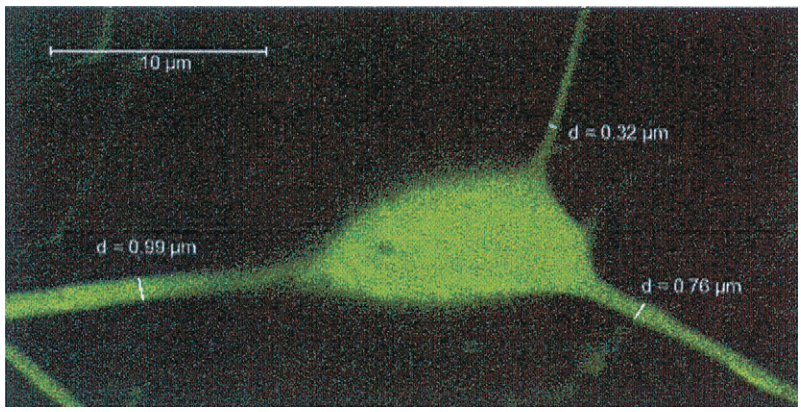


FIGURE 3 Confocal laser scanning micrograph of a cultured neuron (mitral cell) of the OB stained with fluoresceindiacetate.

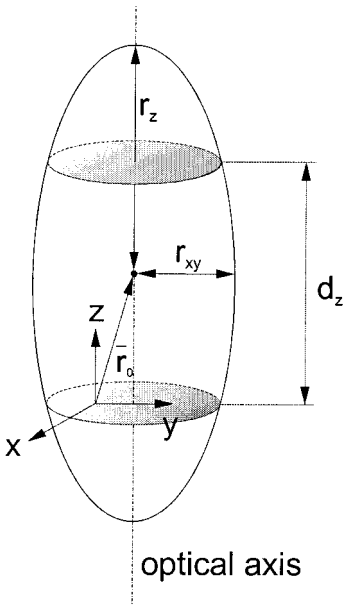


FIGURE 4 Quasi-ellipsoid detection volume $V_d$, characterized by the $1/e^2$-radii $r_{xy}$ and $r_z$, confined in axial direction by boundary planes at $z = z_0 \pm d_z/2$. With respect to the origin ($x = 0$, $y = 0$, $z = 0$), the detection volume of the confocal setup is centered at $\bar{r}_0 = (x_0, y_0, z_0)$.

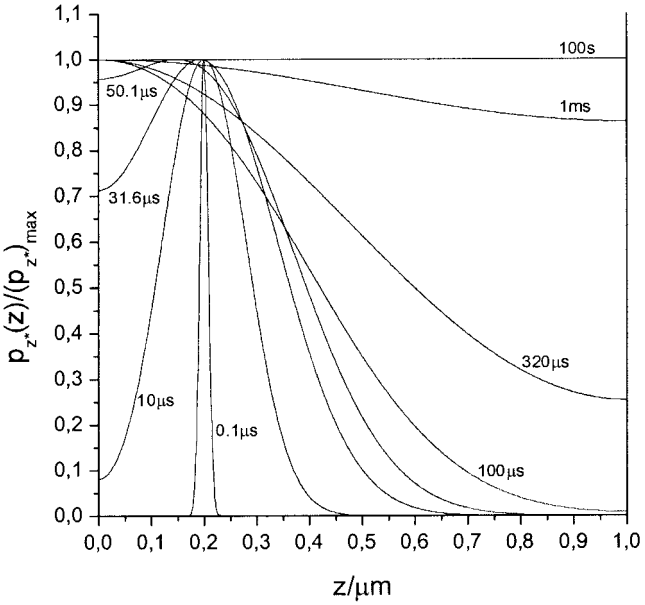


FIGURE 5 Normalized probability density $p_{z*}(z)$ for a single molecule whose diffusion is confined to the space between boundary planes at $z = 0$ $\mu$m and $z = 1$ $\mu$m ($d_z = 1$ $\mu$m), plotted for different times $\tau$ after the start of the random walk at $z' = 0.2$ $\mu$m ($D = 2.8 \times 10^{-6}$ cm$^2$/s).

is the 2D Fokker–Planck solution, and

$$p_{z*}(z, z', \tau) = \frac{1}{d_z} \sum_{m=-\infty}^{\infty} e^{-D\tau(m\pi/d_z)^2} \cos\left(\frac{m\pi z}{d_z}\right) \cos\left(\frac{m\pi z'}{d_z}\right)$$

gives the one-dimensional probability density of a molecule whose random walk is confined to the space between the boundary planes. Figure 5 shows the normalized function $p_{z*}$ (Eq. 26) for a number of values of $\tau$. Note that $p_{z*}$ stays finite for $\tau \to \infty$.

The autocorrelation function $G(\tau)$ of the fluorescence signal $i(t)$,

$$i(t) = \int_{-\infty}^{+\infty} dx \int_{-\infty}^{+\infty} dy \int_0^{d_z} dz\, I_E(\vec{r} - \vec{r}_0) C(\vec{r}, t), \quad (27)$$

with $\vec{r}_0 = (0, 0, z_0)$ being the center of the detection volume, is given by

$$G_{xyz*}(\tau) = \frac{\langle \delta i(0) \delta i(\tau) \rangle}{\langle i \rangle^2} = \frac{G'_{xyz*}(\tau)}{\langle i \rangle^2} = \frac{1}{\langle i \rangle^2} \int_{-\infty}^{+\infty} \int_{-\infty}^{+\infty} dx dx' \int_{-\infty}^{+\infty} \int_{-\infty}^{+\infty} dy dy' \int_0^{d_z} \int_0^{d_z} dz dz' I_E(\vec{r} - \vec{r}_0) I_E(\vec{r}' - \vec{r}_0) \phi(\vec{r}, \vec{r}', \tau), \quad (28)$$

where $G'_{xyz*}(\tau) := \langle \delta i(0) \delta i(\tau) \rangle$ is the unnormalized autocorrelation function, and $z*$ denotes the axis along which diffusion is confined.

Using Eq. 3 and Eq. 24, integrations over $x, x'$ and $y, y'$ give

$$G'_{xyz*}(\tau) = \frac{\langle C \rangle (gQI_0)^2}{4 d_z} \times \frac{\pi r_{xy}^2}{1 + 4D\tau/r_{xy}^2} \int_0^{d_z} \int_0^{d_z} dz dz' \exp\left(-2\frac{(z - z_0)^2}{r_z^2}\right) \exp\left(-2\frac{(z' - z_0)^2}{r_z^2}\right) \times \left[1 + 2 \sum_{m=1}^{\infty} \exp\left[-D\tau\left(\frac{m\pi}{d_z}\right)^2\right] \cos\left(\frac{m\pi z}{d_z}\right) \cos\left(\frac{m\pi z'}{d_z}\right)\right]. \quad (29)$$

Using the normalized variable $\zeta := z/d_z$ and the error function

$$\mathrm{erf}(x) = \frac{2}{\sqrt{\pi}} \int_0^x e^{-t^2} dt, \quad (30)$$

$G'_{xyz*}(\tau)$ takes the form

$$G'_{xyz*}(\tau) = \frac{\langle C\rangle (gQI_0)^2}{4d_z} \times \frac{\pi r_{xy}^2}{1+4D\tau/r_{xy}^2}\left[\frac{\pi r_z^2}{8}\left\{\mathrm{erf}\left[\frac{\sqrt{2}}{r_z}(d_z - z_0)\right] + \mathrm{erf}\left(\frac{\sqrt{2}}{r_z}z_0\right)\right\}^2 + 2d_z^2\sum_{m=1}^{\infty}\exp\left[-D\tau\left(\frac{m\pi}{d_z}\right)^2\right]\left\{\int_0^1 d\zeta \exp\left[-2\left(\frac{d_z}{r_z}\right)^2\left(\zeta - \frac{z_0}{d_z}\right)^2\right]\cos(m\pi\zeta)\right\}^2\right]. \quad (31)$$

To obtain the normalized autocorrelation function $G_{xyz*}(\tau)$, we first calculate the average fluorescence signal $\langle i\rangle$,

$$\langle i\rangle = gQI_0\langle C\rangle \int_{-\infty}^{+\infty}\int_{-\infty}^{+\infty} dx\, dy \exp\left(-2\frac{x^2+y^2}{r_{xy}^2}\right) \int_0^{d_z} dz \exp\left(-2\frac{(z-z_0)^2}{r_z^2}\right) = gQI_0\langle C\rangle \frac{\pi^{3/2}}{2^{5/2}} r_{xy}^2 r_z \left\{\mathrm{erf}\left[\frac{\sqrt{2}}{r_z}(d_z - z_0)\right] + \mathrm{erf}\left(\frac{\sqrt{2}}{r_z}z_0\right)\right\}, \quad (32)$$

and then obtain

$$G_{xyz*}(\tau) = \frac{G'_{xyz*}(\tau)}{\langle i\rangle^2} = \frac{1}{\pi r_{xy}^2 d_z\langle C\rangle}\cdot\frac{1}{1+4D\tau/r_{xy}^2} \times\left\{1 + \frac{16}{\pi}\left(\frac{d_z}{r_z}\right)^2\cdot\frac{\mathcal{A}}{\mathcal{B}}\right\}. \quad (33)$$

where

$$\mathcal{A} = \sum_{m=1}^{\infty}\exp\left(-D\tau\left(\frac{m\pi}{d_z}\right)^2\right) \times\left\{\int_0^1 d\zeta\exp\left[-2\left(\frac{d_z}{r_z}\right)^2\left(\zeta - \frac{z_0}{d_z}\right)^2\right]\cos(m\pi\zeta)\right\}^2$$

$$\mathcal{B} = \left\{\mathrm{erf}\left[\frac{\sqrt{2}}{r_z}(d_z - z_0)\right] + \mathrm{erf}\left(\frac{\sqrt{2}}{r_z}z_0\right)\right\}^2.$$

Using the definition

$$g_{z*}(\tau) := \frac{\sqrt{\pi}r_z}{d_z}\left[1 + \frac{16}{\pi}\left(\frac{d_z}{r_z}\right)^2\cdot\frac{\mathcal{A}}{\mathcal{B}}\right] \quad (34)$$

simplifies the expression for $G_{xyz*}(\tau)$,

$$G_{xyz*}(\tau) = \frac{1}{\pi^{3/2}r_{xy}^2 r_z\langle C\rangle}\cdot\frac{1}{1+4D\tau/r_{xy}^2}\cdot g_{z*}(\tau). \quad (35)$$

We have thus derived an autocorrelation function that is proportional to the 2D autocorrelation function (Eq. 2) times a function $g_{z*}(\tau)$, which accounts for the confined diffusion in axial direction. $g_{z*}(\tau)$ is such that Eq. 35 approaches the 2D model $G_{xy}(\tau)$ (Eq. 2b) for a sufficiently small confinement parameter $d_z/r_z$, while it tends to the 3D model $G_{xyz}(\tau)$ (Eq. 1d) for a sufficiently large confinement parameter $d_z/r_z$. Below, we will quantitatively analyze what exactly is meant by "sufficiently" (see Discussion).

## Diffusion model with boundaries in two dimensions

Neuronal processes such as axons or dendrites often have diameters of one micrometer or less. In these cases, diffusion is usually confined along the optical axis and, in addition, orthogonally to the process, i.e., in $z$- and in $y$-direction. Let us therefore assume additional boundary planes perpendicular to the $y$-axis localized at $y = 0$ and $y = d_y$. Then, following the same line of thought as above, and applying the above steps (Eqs. 28 through 35) results in an autocorrelation function for diffusion confined in $y$- and $z$-direction,

$$G_{xy*z*}(\tau) = \frac{1}{\pi^{3/2}r_{xy}^2 r_z\langle C\rangle}\cdot\frac{1}{\sqrt{1+4D\tau/r_{xy}^2}} \times g_{y*}(\tau)\cdot g_{z*}(\tau), \quad (36)$$

with $g_{y*}(\tau)$ defined in analogy to $g_{z*}(\tau)$ (Eq. 34),

$$g_{y*}(\tau) := \frac{\sqrt{\pi}r_{xy}}{d_y}\left[1 + \frac{16}{\pi}\left(\frac{d_y}{r_{xy}}\right)^2\cdot\frac{\mathcal{C}}{\mathcal{D}}\right]. \quad (37)$$

where

$$\mathcal{C} = \sum_{n=1}^{\infty}\exp\left(-D\tau\left(\frac{n\pi}{d_y}\right)\right)^2 \times\left\{\int_0^1 d\eta\exp\left[-2\left(\frac{d_y}{r_{xy}}\right)^2\left(\eta - \frac{y_0}{d_y}\right)^2\right]\cos(n\pi\eta)\right\}^2$$

$$\mathcal{D} = \left\{\mathrm{erf}\left[\frac{\sqrt{2}}{r_{xy}}(d_y - y_0)\right] + \mathrm{erf}\left(\frac{\sqrt{2}}{r_{xy}}y_0\right)\right\}^2.$$

If diffusion in $z$-direction can be neglected ($g_{z*} \rightarrow \pi^{1/2} r_z/d_z$ for $d_z \rightarrow 0$), while diffusion in $y$-direction cannot be neglected, the adequate diffusion model is

$$G_{xy*}(\tau) = \frac{1}{\pi r_{xy}^2 d_z \langle C\rangle} \cdot \frac{1}{\sqrt{1 + 4D\tau/r_{xy}^2}} \cdot g_{y*}(\tau). \quad (38)$$

The effect of confinement of diffusion in the $y$-direction is illustrated in Fig. 6 for a number of values $d_y/r_{xy}$. Assuming $r_{xy} = 0.25$ $\mu$m and a dendritic diameter of 1 $\mu$m, i.e., $d_y/r_{xy} = 4$, there is a marked deviation of $G_{xy*}(\tau)$ from $G_{xy}(\tau)$ for large $\tau$. In thinner dendrites, the deviation becomes increasingly larger and can also be observed at small $\tau$. These results clearly show the necessity for taking into account the size of the dendritic compartment. However, handling Eq. 34 or Eq. 37 is highly cumbersome. In practical applications, it is presently easier and faster to use an approximation of the modified diffusion model.

## Approximation of $g_{i*}(\tau)$

We were unable to find a closed form expression $\bar{g}_{i*}(\tau)$ that approximates $g_{i*}(\tau)$ for all $d_i/r_i$. However, for $d_i/r_i \leq 8$, the following approximations can be used:

$$\bar{g}_{y*}(\tau) = \frac{\sqrt{\pi}}{Y}\left[1 + \left(\frac{Y}{\sqrt{\pi}} \cdot \frac{\mathrm{erf}(Y)}{\mathrm{erf}^2(Y/\sqrt{2})} - 1\right) \cdot \frac{\exp[-k(Y)(\pi/Y)^2\tau/\tau_{diff}]}{\sqrt{1 + \tau/\tau_{diff}}}\right], \quad (39)$$

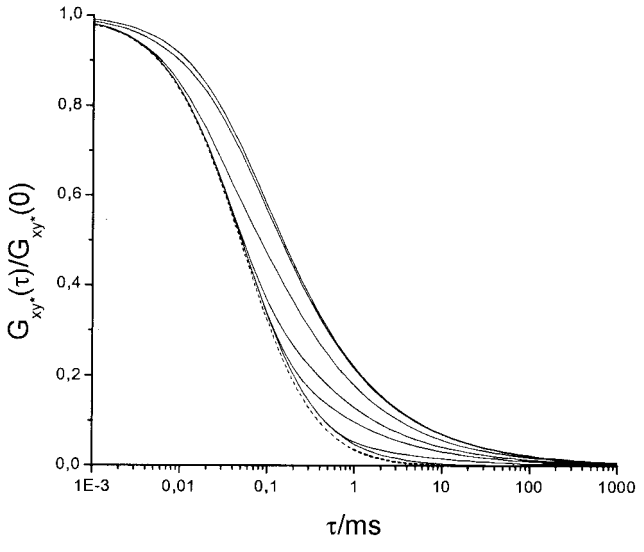


FIGURE 6 Normalized ACF $G_{xy*}(\tau)$ (Eq. 38) for a number of values $Y = d_y/r_{xy}$. The upper six traces correspond, from the upper to the lower curve, to the parameters $Y = 0$, 1, 2, 3, 4 and $Y = 8$. The lowest solid curve shows the normalized trace for $G_{xy*}(\tau)$ for $Y \rightarrow \infty$. For comparison, we have included the normalized ACF $G_{xyz}(\tau)$ (Eq. 1d, *lowest curve*, *dashed*). Parameters: $D = 2.8 \times 10^{-6}$ cm$^2$/s, $r_{xy} = 0.25$ $\mu$m, $S = 5$.

and

$$\bar{g}_{z*}(\tau) = \frac{\sqrt{\pi}}{Z}\left[1 + \left(\frac{Z}{\sqrt{\pi}} \cdot \frac{\mathrm{erf}(Z)}{\mathrm{erf}^2(Z/\sqrt{2})} - 1\right) \cdot \frac{\exp[-k(Z)(\pi/(S \cdot Z))^2\tau/\tau_{diff}]}{\sqrt{1 + \tau/S^2\tau_{diff}}}\right], \quad (40)$$

with

$$k(i) = 0.689 + 0.34 \cdot \exp[-0.37 \cdot (i - 0.5)^2]. \quad (41)$$

An alternative and faster possibility of fitting $g_{i*}(\tau)$ that does not require the calculation of error functions is

$$\bar{g}_{y*}(\tau) = \frac{\sqrt{\pi}}{Y} \cdot \begin{cases} \left[1 + \frac{Y^4}{45}(1 - 0.1004Y^2 + 0.00361Y^4)\exp\left(-\left(\frac{\pi}{Y}\right)^2 \frac{\tau}{\tau_{diff}}\right)\right], & \text{for} \quad Y \in [0, 3.1] \\ \left[1 + \left(\frac{Y}{\sqrt{\pi}} - 1\right)\frac{\exp(-(0.83\pi/Y)^2\tau/\tau_{diff})}{\sqrt{1 + \tau/\tau_{diff}}}\right], & \text{for} \quad Y \in [3.1, 8] \end{cases} \quad (42)$$

and

$$\bar{g}_{z*}(\tau) = \frac{\sqrt{\pi}}{Z} \cdot \begin{cases} \left[1 + \frac{Z^4}{45}(1 - 0.1004Z^2 + 0.00361Z^4)\exp\left(-\left(\frac{\pi}{S \cdot Z}\right)^2 \frac{\tau}{\tau_{diff}}\right)\right], & \text{for} \quad Z \in [0, 3.1] \\ \left[1 + \left(\frac{Z}{\sqrt{\pi}} - 1\right)\frac{\exp(-(0.83\pi/(S \cdot Z))^2\tau/\tau_{diff})}{\sqrt{1 + \tau/S^2\tau_{diff}}}\right], & \text{for} \quad Z \in [3.1, 8]. \end{cases} \quad (43)$$

In either case, the maximum error between the exact function $g_{i*}(\tau)$ and the approximation $\bar{g}_{i*}(\tau)$ is 0.1% for $d_i/r_i < 2$, 1% for $d_i/r_i < 3.1$, 1.2% for $d_i/r_i < 7.7$, and 1.4% for $d_i/r_i \leq 8$, for $i = y$ or $i = z$.

For the approximated ACFs $G_{x\bar{y}*\bar{z}*}(\tau)$ and $G_{x\bar{y}*}(\tau)$, we thus have

$$G_{x\bar{y}*\bar{z}*}(\tau) = \frac{1}{V_d\langle C\rangle} \cdot \frac{1}{\sqrt{1 + \tau/\tau_{diff}}} \cdot \bar{g}_{y*}(\tau) \cdot \bar{g}_{z*}(\tau), \quad (44)$$

and

$$G_{x\bar{y}*}(\tau) = \frac{1}{V_{cyl.}\langle C\rangle} \cdot \frac{1}{\sqrt{1 + \tau/\tau_{diff}}} \cdot \bar{g}_{y*}(\tau), \quad (45)$$

with $V_{cyl.} := \pi r_{xy}^2 d_z$.

We will now apply the ACF $G_{x\bar{y}*}(\tau)$ to experimental data.

### Application of the diffusion model $G_{xy*}(\tau)$

We loaded OB neurons with TMR-dextran (10 kDa, see Methods) and carried out FCS measurements on dendrites with diameters of 1 $\mu$m or less. Diffusion in the axial direction can be neglected because, with $r_{xy} = 0.24$ $\mu$m and $S = 7$, we have $r_z = 1.7$ $\mu$m, i.e., the dendritic diameter is sufficiently smaller than the height of the detection volume (see Discussion). In the radial direction, however, lateral diffusion is confined by the dendritic boundaries at $y = \pm d_y/2 \leq \pm 0.5$ $\mu$m that cut away a part of the open detection volume. Moreover, in living cells, we have to consider more than one characteristic diffusion time (Brock et al., 1998), so that the modified ACF model is given by

$$G(\tau) = \frac{1}{\langle N_{ges}\rangle}\left(1 - \frac{I_B}{I_{tot}}\right)^2\left(1 + \frac{Te^{-\tau/\tau_T}}{1-T}\right) \times \sum_{j=1}^{m} \Phi_j \cdot g_x^j(\tau) \cdot \bar{g}_{y*}^j(\tau), \quad (46)$$

with $m$ standard ACF terms for diffusion along the dendrite, i.e., the $x$-axis,

$$g_x^j(\tau) := \frac{1}{\sqrt{1 + \tau/\tau_{diff_j}}}, \quad (47)$$

and $m$ approximated ACF terms for confined diffusion along the $y$-axis (Eq. 39)

$$\bar{g}_{y*}^j(\tau) := \frac{\sqrt{\pi}}{Y}\left[1 + \left(\frac{Y}{\sqrt{\pi}} \cdot \frac{\mathrm{erf}(Y)}{\mathrm{erf}^2(Y/\sqrt{2})} - 1\right) \times \frac{\exp[-k(Y)(\pi/Y)^2\tau/\tau_{diff_j}]}{\sqrt{1 + \tau/\tau_{diff_j}}}\right]. \quad (48)$$

In Fig. 2 we have shown that the standard diffusion model is not sufficient to describe experimental data taken from a dendrite. We now apply the modified ACF model (Eq. 46) to the same experimental data (Fig. 2). The fit nicely converges giving two components: $\Phi_1 = 0.34$, $\tau_{diff_1} = 0.187$ ms, $\Phi_2 = 0.66$ and $\tau_{diff_2} = 2.11$ ms (Fig. 7). The fit parameter $Y$ resulted to be $Y = 3.576$ corresponding to a dendritic diameter $d_y = r_{xy} \cdot Y = 0.84$ $\mu$m ($r_{xy} = 0.236$ $\mu$m). This is in good agreement with the line-scanning measurement of the dendrite, which gave a diameter of 0.81 $\mu$m. One of the time constants was always found to be in the range 180–300 $\mu$s. The same value also resulted from measurements in the soma using Eq. 1b as diffusion model. In 55 somata the predominant diffusion time constant was in the range of 200–350 $\mu$s.

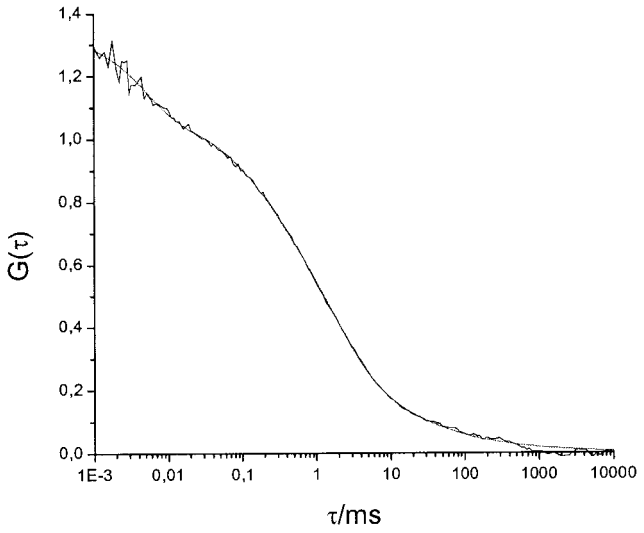


FIGURE 7 ACF of the fluorescence fluctuation data shown in Fig. 2, together with the modified ACF model (Eq. 46). The experimental ACF was calculated over 60 s from the fluorescence fluctuations of 10 kDa TMR-dextran emitted from a dentrite of a cultured neuron. Result of the fit: $\langle N\rangle = 0.939$, $T = 0.202$, and $\tau_T = 5.01$ $\mu$s. $\Phi_1$, $\Phi_2$, $\tau_{diff_1}$, $\tau_{diff_2}$, and $Y$ are explained in the text.

In water, $\tau_{diff}$ of the TMR-dextran (10 kDa) was 160 $\mu$s $\pm$ 6 $\mu$s. Taken together the time constant in the range 180–350 $\mu$s clearly appears to be the principal time constant of TMR-dextran (10 kDa) in the cytosol.

In the above case, where the standard model led to a characteristic time constant smaller than that in water, the values coming out from the standard model were obviously wrong. However, in other cases where there were two components $\Phi_1$ and $\Phi_2$, it was a priori not clear that these values were erroneous. Figure 8 shows data of this type measured in a dendrite with a diameter of $d_y = 0.63$ $\mu$m (line-scanning measurement). The standard model (Eq. 1b) led to $\Phi_1 = 0.84$, $\tau_{diff_1} = 0.536$ ms and $\Phi_2 = 0.16$, $\tau_{diff_2} = 46.37$ ms. As the dendritic boundaries severely confine the diffusion space, these results must be supposed to be wrong. In fact, applying the modified model led to $\Phi_1 = 0.31$, $\tau_{diff_1} = 0.25$ ms, $\Phi_2 = 0.69$, $\tau_{diff_2} = 1.03$ ms, and $Y = d_y/r_{xy} = 2.712$, i.e., $d_y = 2.712 \cdot 0.236$ $\mu$m $= 0.64$ $\mu$m. $\tau_{diff_1}$ was thus exactly in the expected range, and $d_y$ was virtually the same value as the one obtained by line scanning through the dendrite.

## DISCUSSION

The major application of FCS is measuring low concentrations and diffusion constants. The detection volume is usually given by the excitation volume of a focused laser together with a confocal emission pathway. A problem occurs if the diffusion space is confined by boundaries such as a plasma membrane so that the diffusion takes place in a volume that is comparable

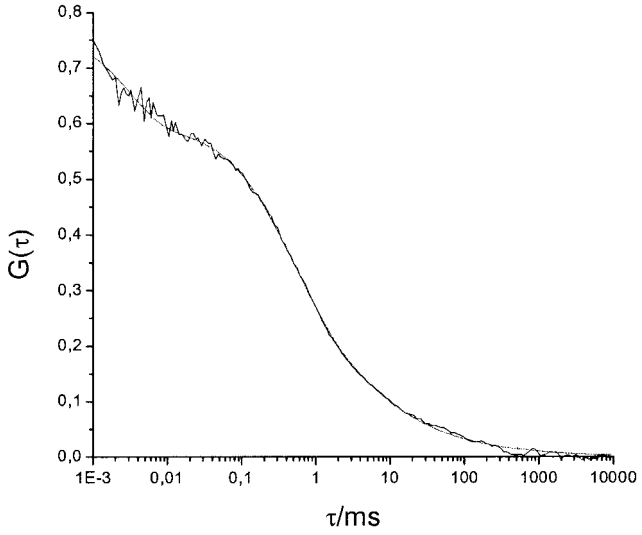


FIGURE 8 Autocorrelation function calculated from fluorescence fluctuations of 10 kDa TMR-dextran emitted from a dentrite of a cultured neuron of the OB. The intracellular dye concentration was 20 nM. Data were gathered over 60 s. The smooth curve shows the fit of the data to the modified ACF model (Eq. 46). Result of the fit: $\langle N\rangle = 1.7$, $T = 0.225$, $\tau_T = 3.15\ \mu$s, and $\Phi_1$, $\Phi_2$, $\tau_{diff_1}$, $\tau_{diff_2}$, and $Y$ as given in the text.

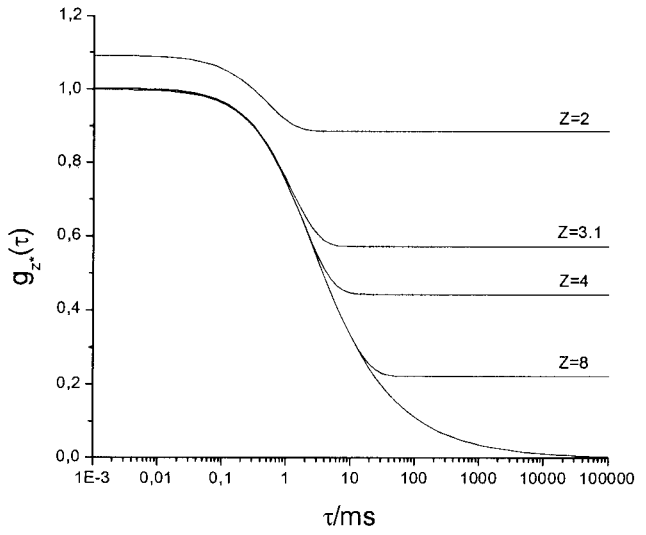


FIGURE 9 Modified one-dimensional autocorrelation function $g_{z*}(\tau)$ (Eq. 34) for a number of values $Z = d_z/r_z$. The lowest curve shows the modified model $g_{z*,\infty}(\tau)$ for unconfined diffusion. It is undistinguishable from $g_z(\tau) = (1 + 4D\tau/r_z^2)^{-1/2}$ (also drawn). Parameters: $D = 2.8 \times 10^{-6}$ cm$^2$/s, $r_{xy} = 0.25\ \mu$m, $S = 5$.

with or smaller than the confocal detection volume. We have shown herein that, in such cases, the standard FCS diffusion models lead to erroneous results, e.g., the false detection of fluorescent species and wrong values for the characteristic diffusion times. We have developed a novel model that takes boundaries explicitly into account.

Our model allows determination of the limits within which the standard 2D diffusion is valid, i.e., how small a compartment has to be so that, using the standard 2D model, the error does not exceed a given value. In a similar way, we will calculate the limits within which the standard 3D model is valid, i.e., which size a compartment has to exceed so that, using the 3D model, the error is smaller than a given value.

Another point that needs to be discussed here is the volume of the diffusion space. To calculate a concentration, one needs the volume in addition to the average particle number $\langle N\rangle$ which follows from the model.

## $Z-$limit of the 2D diffusion model $G_{xy}(\tau)$

The standard 2D diffusion model reflects experimental autocorrelation functions correctly if $d_z/r_z$ is sufficiently small. The range $[0, (d_z/r_z)_{max}]$, for which this is the case, follows from Eq. 34. It can easily be seen that $g_{z*}(\tau)$ starts with values larger than $\pi^{1/2}r_z/d_z$ for small $\tau$ and approaches $\pi^{1/2}r_z/d_z$ for $\tau \to \infty$. If we accept 1% deviation of $G_{xyz*}(\tau)$ from $G_{xy}(\tau)$, $g_{z*}(\tau)$ must be smaller than $1.01 \cdot \pi^{1/2}r_z/d_z$ for all $\tau$. As $g_{z*}(\tau)$ has its maximum at $\tau = 0$ (see Fig. 9), this condition is $g_{z*}(0) \le 1.01 \cdot \pi^{1/2}r_z/d_z$. With the detection volume centered at $z_0 \equiv d_z/2$, we have for $g_{z*}(0)$ (Eq. 34)

$$
\begin{aligned}
&g_{z*}(0)\\
&= \frac{\sqrt{\pi}r_z}{d_z}\left[1 + \frac{4}{\pi}\left(\frac{d_z}{r_z}\right)^2 \frac{\sum_{m=1}^{\infty}\left\{\int_0^1 d\zeta \exp\left[-2\left(\frac{d_z}{r_z}\right)^2\left(\zeta - \frac{1}{2}\right)^2\right]\cos(m\pi\zeta)\right\}^2}{[\mathrm{erf}(d_z/\sqrt{2}r_z)]^2}\right]\\
&= \frac{2d_z}{\sqrt{\pi}r_z}\cdot\frac{\sum_{m=-\infty}^{\infty}\left\{\int_0^1 d\zeta \exp\left[-2\left(\frac{d_z}{r_z}\right)^2\left(\zeta - \frac{1}{2}\right)^2\right]\cos(m\pi\zeta)\right\}^2}{[\mathrm{erf}(d_z/\sqrt{2}r_z)]^2}\\
&= \frac{2d_z}{\sqrt{\pi}r_z}\cdot\frac{\sum_{m=-\infty}^{\infty}|c_m|^2}{[\mathrm{erf}(d_z/\sqrt{2}r_z)]^2},
\end{aligned}
\tag{49}
$$

where the $c_m$ are the Fourier coefficients of $f(\zeta)$

$$
f(\zeta) := \exp\left[-2\left(\frac{d_z}{r_z}\right)^2\left(\zeta - \frac{1}{2}\right)^2\right], \tag{50}
$$

i.e.,

$$
c_m = \int_0^1 d\zeta\, f(\zeta)\cos(2m\pi\zeta). \tag{51}
$$

For $z_0 \equiv d_z/2$, the integral in Eq. 49 vanishes for odd numbers $m$. We therefore replaced $m$ with $2m$.

Using Parseval's Theorem,

$$\sum_{m=-\infty}^{\infty} |c_m|^2 = \int_0^1 |f(\zeta)|^2 \, d\zeta$$

$$= \int_0^1 \exp\left[-4\left(\frac{d_z}{r_z}\right)^2\left(\zeta - \frac{1}{2}\right)^2\right] d\zeta$$

$$= \frac{\sqrt{\pi} r_z}{2d_z} \cdot \mathrm{erf}\left(\frac{d_z}{r_z}\right), \tag{52}$$

Eq. 49 takes the form

$$g_{z^*}(0) = \frac{\mathrm{erf}(d_z/r_z)}{[\mathrm{erf}(d_z/\sqrt{2}r_z)]^2}. \tag{53}$$

Simple numerical analysis shows that the inequality $g_{z^*}(0) \le 1.01 \cdot \pi^{1/2} r_z/d_z$ holds for $d_z/r_z \le 0.833$. Given a typical waist radius $r_{xy} = 0.25$ $\mu$m and a typical structure factor of $S = 5$, we have $r_z = 1.25$ $\mu$m and $d_z = 1.04$ $\mu$m. For cellular compartments that do not exceed 1 $\mu$m in height, diffusion in axial direction can thus be neglected. Provided that diffusion is not confined in radial direction, the standard 2D diffusion model is adequate. In case diffusion is additionally confined in one dimension of the image plane, the modified model $G_{xy^*}(\tau)$ needs to be applied.

### *Z*—limit of the 3D diffusion model $G_{xyz}(\tau)$

We now discuss the question of which size (in axial direction) a cell must exceed so that the 3D diffusion model $G_{xyz}(\tau)$ is appropriate. In other words, what is the limit $(d_z/r_z)_{min}$ so that, for all $(d_z/r_z) \ge (d_z/r_z)_{min}$, the relative deviation $\beta$ of the 3D model $G_{xyz}(\tau)$ (Eq. 1d) from the modified model $G_{xyz^*}(\tau)$ (Eq. 35) never exceeds a certain value? Because the relative deviation $\beta$ is a monotonically increasing function of $\tau$, we have to choose a value $\tau_1$, so that, for $\tau \le \tau_1$, the 3D model $G_{xyz}(\tau)$ deviates less than $\beta$ from the modified model $G_{xyz^*}(\tau)$. Let us choose $\tau_1$ so that $G_{xyz}(\tau_1) := \alpha G_{xyz}(0)$ equals 10% ($\alpha = 0.1$) of its initial amplitude, $G_{xyz}(\tau_1) := 0.1\ G_{xyz}(0)$. We are thus asking for which parameter $(d_z/r_z)_{min}$ the function $G_{xyz^*}(\tau)$ assumes a value such that $G_{xyz^*}(\tau_1) = (1 + \beta)G_{xyz}(\tau_1)$, where $\beta$ is given by

$$\beta = \frac{G_{xyz^*}(\tau_1) - G_{xyz}(\tau_1)}{G_{xyz}(\tau_1)} = \frac{g_{z^*}(\tau_1) - g_z(\tau_1)}{g_z(\tau_1)} = \frac{g_{z^*}(\tau_1)}{g_z(\tau_1)} - 1. \tag{54}$$

As can clearly be seen from Fig. 9, $g_{z^*}(\tau)$ approaches the function

$$g_{z^*,\infty}(\tau) := \lim_{d_z/r_z \to \infty} g_{z^*}(\tau) = \frac{1}{\sqrt{1 + 4D\tau/r_z^2}} = g_z(\tau) \tag{55}$$

for $d_z/r_z \to \infty$. If we accept an error $\beta$ of 1%, it follows that $g_{z^*}(\tau_1)$ must fulfill the equation

$$g_{z^*}(\tau_1) = 1.01 \cdot g_z(\tau_1). \tag{56}$$

Numerical analysis of Eq. 56 shows that, for a typical structure factor of $S = 5$ and $z_0 \equiv d_z/2$, this is true for $(d_z/r_z)_{min} = 2.87$. Given a typical waist radius of $r_{xy} = 0.25$ $\mu$m, we obtain $(d_z)_{min} = 2.87 \cdot r_z = 2.87 \cdot S \cdot r_{xy} = 3.59$ $\mu$m.

Hence, if the distance between the cellular boundaries in $z$-direction is larger than 3.59 $\mu$m, the 3D standard diffusion model gives a correct interpretation of experimental data for $\tau \le \tau_1$ and within an error of 1%.

### *Y*—limit of the 2D diffusion model $G_{xy}(\tau)$

In most neuronal processes, diffusion in axial direction can be neglected (see subsection "Z-limit of the 2D diffusion model $G_{xy}(\tau)$"). This means we have to use either the standard 2D model $G_{xy}(\tau)$, in case diffusion is not confined in $y$-direction, or the modified model $G_{xy^*}(\tau)$ (Eq. 38), otherwise. Which diameter $(d_y)_{min}$ must a process exceed so that the 2D diffusion model $G_{xy}(\tau)$ is appropriate? In other words, what is the limit $(d_y/r_{xy})_{min}$ so that, for all $(d_y/r_{xy}) \ge (d_y/r_{xy})_{min}$, the relative deviation $\beta$ of the 2D model $G_{xy}(\tau)$ from the modified model $G_{xy^*}(\tau)$ never exceeds a certain value? Because the relative deviation $\beta$ is a monotonically increasing function of $\tau$, we have to choose a value $\tau_1$, so that, for $\tau \le \tau_1$ the 2D model deviates less than $\beta$ from the modified model. Let us choose $\tau_1$ so that $G_{xy}(\tau_1) := \alpha G_{xy}(0)$ equals 10% ($\alpha = 0.1$) of its initial amplitude, i.e., $G_{xy}(\tau_1) = 0.1\ G_{xy}(0)$. We are thus asking for which parameter $(d_y/r_{xy})_{min}$ the function $G_{xy^*}(\tau)$ assumes a value such that $G_{xy^*}(\tau_1) = (1 + \beta)G_{xy}(\tau_1)$. With Eq. 2b and 38, we obtain, for $\beta$

$$\beta = \frac{G_{xy^*}(\tau_1) - G_{xy}(\tau_1)}{G_{xy}(\tau_1)} = \frac{g_{y^*}(\tau_1) - g_y(\tau_1)}{g_y(\tau_1)} = \frac{g_{y^*}(\tau_1)}{g_y(\tau_1)} - 1 \tag{57}$$

If we accept an error $\beta$ of 1%, it follows that $g_{y^*}(\tau_1)$ must fulfill the equation

$$g_{y^*}(\tau_1) = 1.01 g_y(\tau_1). \tag{58}$$

Numerical analysis of Eq. 58 shows that, for $y_0 \equiv d_y/2$, this is true for $(d_y/r_{xy})_{min} = 7.28$, i.e., $d_y = 1.8$ $\mu$m for a typical waist radius of 0.25 $\mu$m. Hence, if the diameter of a cellular process is thicker than 1.8 $\mu$m, the 2D standard diffusion model gives correct interpretation of experimental data for $\tau \le \tau_1$ and within an error of 1%.

In conclusion, because most neuronal processes are thinner than 1.8 $\mu$m, the modified model for confined diffusion should be used. Table 1 gives an overview of the various

**TABLE 1 Appropriate ACF models for confined diffusion along the *y*- and *z*-axes**

| | $Z \le 0.833$ | $\forall Z$ | $Z \le 8$ | $Z \to \infty$ | $Z > 2.87$, $\alpha = 0.1$, $S = 5$ | $Z > 4.12$, $\alpha = 0.01$, $S = 5$ |
|---|---|---|---|---|---|---|
| $Y \le 0.833$ | $G_{x}(\tau)$ | $G_{xz*}(\tau)$ | $G_{x\bar{z}*}$ | $G_{xz}(\tau)$ | — | — |
| $\forall Y$ | $G_{xy*}(\tau)$ Eq. 38 | $G_{xy*z*}(\tau)$ Eq. 36 | $G_{xy*\bar{z}*}(\tau)$ | $G_{xy*z}(\tau)$ | — | — |
| $Y \le 8$ | $G_{x\bar{y}*}(\tau)$ Eq. 45 | $G_{x\bar{y}*z*}(\tau)$ | $G_{x\bar{y}*\bar{z}*}(\tau)$ Eq. 44 | $G_{x\bar{y}*z}(\tau)$ | — | — |
| $Y \to \infty$ | $G_{xy}(\tau)$ Eq. 2b | $G_{xyz*}(\tau)$ Eq. 35 | $G_{xy\bar{z}*}(\tau)$ | $G_{xyz}(\tau)$ Eq. 1d | $G_{xyz}(\tau)$ Eq. 1d | $G_{xyz}(\tau)$ Eq. 1d |
| $Y > 7.28$, $\alpha = 0.1$ | $G_{xy}(\tau)$ Eq. 2b | — | — | — | — | — |
| $Y > 23$, $\alpha = 0.01$ | $G_{xy}(\tau)$ Eq. 2b | — | — | — | — | — |

ACF models and indicates the appropriate model for the various parameter combinations. The overlined indices denote the approximated part of the ACF, i.e., $\bar{y}*$ stands for $\bar{g}_{y*}(\tau)$ (Eq. 39 or Eq. 42) and $\bar{z}*$ for $\bar{g}_{z*}(\tau)$ (Eq. 40 or Eq. 43), and the nonoverlined indices denote the exact functions, i.e., $y*$ stands for $g_{y*}(\tau)$ (Eq. 37) and $z*$ for $g_{z*}(\tau)$ (Eq. 34), whereby the asterisk indicates axes of confined diffusion. If diffusion occurs in all directions, the detection volume in the ACF is given by $V_d = \pi^{3/2} r_{xy}^2 r_z = \pi^{1/2} r_{xy} \cdot \pi^{1/2} r_{xy} \cdot \pi^{1/2} r_z$. Every direction $i$ thus contributes a factor $\pi^{1/2} r_i$. If the diffusion volume is confined, e.g., in $z$-direction, this is taken into account by the function $g_{z*}(\tau)$. In case of a sufficiently small confinement parameter $d_i/r_i$, i.e., $d_i/r_i \le 0.833$, the corresponding factor $\pi^{1/2} r_i$ of the detection volume is replaced by the distance of the boundary planes $d_i$, because, for $d_i/r_i \le 0.833$, we have $g_{i*}(\tau) \cong \pi^{1/2} r_i/d_i$. For $Z \le 0.833$, the detection volume becomes thus $V_d = \pi^{1/2} r_{xy} \cdot \pi^{1/2} r_{xy} \cdot d_z = \pi r_{xy}^2 d_z = V_{cyl.}$. For confined diffusion in any combination of directions, the ACFs can be built correspondingly.

## Assigning concentrations

The 3D standard diffusion model gives the average number $\langle N \rangle$ of fluorescent molecules in the sample volume as a result of the fit of the model to experimental data. $\langle N \rangle$ is the product of the average concentration $\langle C \rangle$ and the detection volume $V_d = \pi^{3/2} r_{xy}^2 r_z$. The concentration is thus $\langle C \rangle = \langle N \rangle / V_d$. Note that $V_d$ is an open volume so that detection occurs also beyond the characteristic radii $r_{xy}$ and $r_z$.

To find the average concentration $\langle C \rangle$ in the case of confined diffusion, let us evaluate $G_{xyz*}(\tau)$ for $\tau = 0$. Assuming the center of the detection volume at $z_0 \equiv d_z/2$ and, using Eq. 35 and $g_{z*}(0)$ (Eq. 53), we have

$$G_{xyz*}(0) = \frac{1}{\pi^{3/2} r_{xy}^2 r_z \langle C \rangle} \cdot \frac{\mathrm{erf}(d_z/r_z)}{[\mathrm{erf}(d_z/\sqrt{2} r_z)]^2}$$

$$= \frac{1}{V_d^* \langle C \rangle} = \frac{1}{\langle N \rangle}, \tag{59}$$

where $\langle N \rangle = V_d^* \langle C \rangle$ is the number of fluorescent molecules in the effective detection volume $V_d^*$:

$$V_d^* := \pi^{3/2} r_{xy}^2 r_z \cdot \frac{[\mathrm{erf}(d_z/\sqrt{2} r_z)]^2}{\mathrm{erf}(d_z/r_z)}. \tag{60a}$$

Quite expectedly, for $d_z/r_z \to \infty$, the volume tends to the unconfined volume $V_d$,

$$V_d^* \to V_d = \pi^{3/2} r_{xy}^2 r_z, \tag{60b}$$

and for $d_z/r_z \ll 1$, we find a cylinder volume,

$$V_d^* \to V_{cyl.} = \pi r_{xy}^2 d_z, \tag{60c}$$

because $\mathrm{erf}(x) \approx 2x/\pi^{1/2}$ for $x \ll 1$.

Fig. 10 shows the normalized detection volume $V_d^*/V_d$ as a function of $d_z/r_z$. For $d_z/r_z \le 0.835$, the detection volume $V_d^*$ equals, within an error of 1%, the cylinder volume $\pi r_{xy}^2 d_z$, i.e., $V_d^*/V_d \approx \pi^{1/2} d_z/r_z$, and for $d_z/r_z \ge 2.804$ the normalized volume tends to unity. The 3D ACF model $G_{xyz}(\tau)$ (Eq. 1d) with $V_d^* \approx V_d = \pi^{3/2} r_{xy}^2 r_z$ gives reliable concentrations (within 1% error) if $d_z \ge 2.804\, r_z$, while the 2D ACF model $G_{xy}(\tau)$ (Eq. 2b) with $V_d^* \approx V_{cyl.} = \pi r_{xy}^2 d_z$ gives reliable concentrations (within 1% error) for $d_z \le 0.835 r_z$. For distances $d_z$ in the intermediate range, we have to take into account the barrel-shape (see Fig. 4) of the detection volume $V_d^*$ (Eq. 60a) to obtain $\langle C \rangle$.

In case of FCS measurements with $d_z \le 0.835 r_z$, the value $d_z$ cannot be derived from the experimental ACF data.

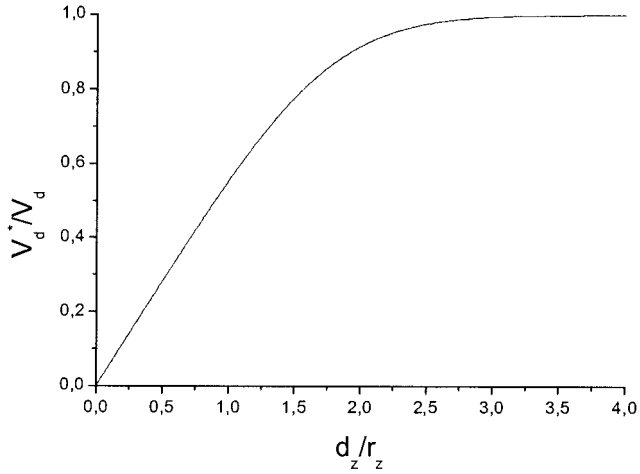


FIGURE 10 Normalized effective detection volume $V_d^*/V_d$ as a function of the confinement parameter $d_z/r_z$.

The volume is thus not known, and $\langle C\rangle$ cannot be calculated from $\langle N\rangle$. However, we can obtain $\langle C\rangle$, using Eq. 60a and line scans through the dendrite (see Methods).

In cases where diffusion is confined in $z$- and $y$-direction, we obtain, using the same arguments as above,

$$G_{xy^*z^*}(0) = \frac{1}{\pi^{3/2} r_{xy}^2 r_z \langle C\rangle} \times \frac{\mathrm{erf}(d_y/r_{xy})}{[\mathrm{erf}(d_y/\sqrt{2}r_{xy})]^2} \cdot \frac{\mathrm{erf}(d_z/r_z)}{[\mathrm{erf}(d_z/\sqrt{2}r_z)]^2}. \quad (61)$$

If $d_y/r_{xy} \leq 0.835$ and $d_z/r_z \leq 0.835$, the detection volume is given by $V_d \approx \pi^{1/2} r_{xy} d_y d_z$. To obtain $\langle C\rangle$ in this case, $d_y$ and $d_z$ need to be measured using another methods, e.g., line scanning.

## REFERENCES


Aragón, S. R., and R. Pecora. 1976. Fluorescence correlation spectroscopy as a probe of molecular dynamics. *J. Chem. Phys.* 64:1791–1803.

Berland, K. M., P. T. C. So, and E. Gratton. 1995. Two-photon fluorescence correlation spectroscopy: method and application to the intracellular environment. *Biophys. J.* 68:694–701.

Bischofberger, J., and D. Schild. 1995. Different spatial patterns of $Ca^{2+}$ increase by N- and L-type $Ca^{2+}$ channel activation in frog olfactory bulb neurones. *J. Physiol.* 487:305–317.

Bischofberger, J., H. Geiling, J. Engel, H. A. Schultens, and D. Schild. 1995. A cultured network of olfactory bulb neurons of *Xenopus laevis* tadpoles: calcium imaging and spontaneous activity. *In* Advances in the Biosciences, Vol. 93, Chemical Signals in Vertebrates, R. Apfelbach, D. Müller-Schwarze, K. Reutter, and E. Weiler, editors. Elsevier, Oxford. 133–139.

Brock, R., M. A. Hink, and T. M. Jovin. 1998. Fluorescence correlation microscopy of cells in the presence of autofluorescence. *Biophys. J.* 75:2547–2557.

Elson, E. L., and D. Magde. 1974. Fluorescence correlation spectroscopy. I. Conceptual basis and theory. *Biopolymers.* 13:1–27.

Koppel, D. E. 1974. Statistical accuracy in fluorescence correlation spectroscopy. *Phys. Rev. A.* 10:1938–1945.

Nieuwkoop, P. D., and J. Faber. 1956. Normal Table of *Xenopus laevis* (*Daudin*). North Holland Company, Amsterdam.

Papoulis, A. 1991. Probability, Random Variables, and Stochastic Processes. Third Edition. McGraw-Hill, New York.

Politz, J. C., E. S. Browne, D. E. Wolf, and T. Pederson. 1998. Intranuclear diffusion and hybridization state of oligonucleotides measured by fluorescence correlation spectroscopy in living cells. *Proc. Natl. Acad. Sci. USA.* 95:6043–6048.

Rigler, R., Ü. Mets, J. Widengren, and P. Kask. 1993. Fluorescence correlation spectroscopy with high count rate and low background: analysis of translational diffusion. *Eur. Biophys. J.* 22:169–175.

Schwille, P., U. Haupts, S. Maiti, and W. W. Webb. 1999. Molecular dynamics in living cells observed by fluorescence correlation spectroscopy with one- and two-photon excitation. *Biophys. J.* 77:2251–2265.

Trombley, P. Q., and G. L. Westbrook. 1990. Excitatory synaptic transmission in cultures of rat olfactory bulb. *J. Neurophysiol.* 64:598–606.

Widengren, J., Ü. Mets, and R. Rigler. 1995. Fluorescence correlation spectroscopy of triplet states in solution: a theoretical and experimental study. *J. Phys. Chem.* 99:13368–13379.

Widengren, J., and R. Rigler. 1998. Fluorescence correlation spectroscopy as a tool to investigate chemical reactions in solutions and on cell surfaces. *Cell. Mol. Biol.* 44:857–879.